

## Updated High-Temperature Opacities for The Dartmouth Stellar Evolution Program and their Effect on the Jao Gap Location

2 THOMAS M. BOUDREAUX<sup>1</sup> AND BRIAN C. CHABOYER<sup>1</sup>

3 <sup>1</sup>*Department of Physics and Astronomy, Dartmouth College, Hanover, NH 03755, USA*

### 4 ABSTRACT

5 The Jao Gap, a 17 percent decrease in stellar density at  $M_G \sim 10$  identified in both Gaia DR2  
6 and EDR3 data, presents a new method to probe the interior structure of stars near the fully con-  
7 vective transition mass. The Gap is believed to originate from convective kissing instability wherein  
8 asymmetric production of  $^3\text{He}$  causes the core convective zone of a star to periodically expand and  
9 contract and consequently the stars' luminosity to vary. Modeling of the Gap has revealed a sensitivity  
10 in its magnitude to a population's metallicity primarily through opacity. Thus far, models of the Jao  
11 Gap have relied on OPAL high-temperature radiative opacities. Here we present updated synthetic  
12 population models tracing the Gap location modeled with the Dartmouth stellar evolution code using  
13 the OPLIB high-temperature radiative opacities. Use of these updated opacities changes the predicted  
14 location of the Jao Gap by  $\sim 0.05$  mag as compared to models which use the OPAL opacities.

15 *Keywords:* Stellar Evolution (1599) — Stellar Evolutionary Models (2046)

### 16 1. INTRODUCTION

17 Due to the initial mass requirements of the molecular  
18 clouds which collapse to form stars, star formation is  
19 strongly biased towards lower mass, later spectral class  
20 stars when compared to higher mass stars. Partly as  
21 a result of this bias and partly as a result of their ex-  
22 tremely long main-sequence lifetimes, M Dwarfs make  
23 up approximately 70 percent of all stars in the galaxy.  
24 Moreover, some planet search campaigns have focused  
25 on M Dwarfs due to the relative ease of detecting small  
26 planets in their habitable zones (e.g. Nutzman & Char-  
27 bonneau 2008). M Dwarfs then represent both a key  
28 component of the galactic stellar population as well as  
29 the possible set of stars which may host habitable ex-  
30 oplanets. Given this key location M Dwarfs occupy in  
31 modern astronomy it is important to have a thorough  
32 understanding of their structure and evolution.

33 Jao et al. (2018) discovered a novel feature in the Gaia  
34 Data Release 2 (DR2)  $G_{BP} - G_{RP}$  color-magnitude-  
35 diagram. Around  $M_G = 10$  there is an approximately  
36 17 percent decrease in stellar density of the sample of

37 stars Jao et al. (2018) considered. Subsequently, this  
38 has become known as either the Jao Gap, or Gaia M  
39 Dwarf Gap. Following the initial detection of the Gap  
40 in DR2 the Gap has also potentially been observed in  
41 2MASS (Skrutskie et al. 2006; Jao et al. 2018); however,  
42 the significance of this detection is quite weak and it re-  
43 lies on the prior of the Gap's location from Gaia data.  
44 Further, the Gap is also present in Gaia Early Data Re-  
45 lease 3 (EDR3) (Jao & Feiden 2021). These EDR3 and  
46 2MASS data sets then indicate that this feature is not  
47 a bias inherent to DR2.

48 The Gap is generally attributed to convective instabil-  
49 ities in the cores of stars straddling the fully convective  
50 transition mass ( $0.3 - 0.35 M_\odot$ ) (Baraffe & Chabrier  
51 2018). These instabilities interrupt the normal, slow,  
52 main sequence luminosity evolution of a star and result  
53 in luminosities lower than expected from the main se-  
54 quence mass-luminosity relation (Jao & Feiden 2020).

55 The Jao Gap, inherently a feature of M Dwarf pop-  
56 ulations, provides an enticing and unique view into the  
57 interior physics of these stars (Feiden et al. 2021). This  
58 is especially important as, unlike more massive stars,  
59 M Dwarf seismology is infeasible due to the short peri-  
60 ods and extremely small magnitudes which both radial  
61 and low-order low-degree non-radial seismic waves are  
62 predicted to have in such low mass stars (Rodríguez-  
63 López 2019). The Jao Gap therefore provides one of the

Corresponding author: Thomas M. Boudreax  
thomas.m.boudreax.gr@dartmouth.edu,  
thomas@boudreauxmail.com

<sup>64</sup> only current methods to probe the interior physics of M  
<sup>65</sup> Dwarfs.

<sup>66</sup> Despite the early success of modeling the Gap some  
<sup>67</sup> issues remain. [Jao & Feiden \(2020, 2021\)](#) identify that  
<sup>68</sup> the Gap has a wedge shape which has not been successful  
<sup>69</sup> reproduced by any current modeling efforts and which  
<sup>70</sup> implies a somewhat unusual population composition of  
<sup>71</sup> young, metal-poor stars. Further, [Jao & Feiden \(2020\)](#)  
<sup>72</sup> identify substructure, an additional over density of stars,  
<sup>73</sup> directly below the Gap, again a feature not yet fully  
<sup>74</sup> captured by current models.

<sup>75</sup> All currently published models of the Jao Gap make  
<sup>76</sup> use of OPAL high temperature radiative opacities. Here  
<sup>77</sup> we investigate the effect of using the more up-to-  
<sup>78</sup> date OPLIB high temperature radiative opacities and  
<sup>79</sup> whether these opacity tables bring models more in line  
<sup>80</sup> with observations. In Section 2 we provide an overview  
<sup>81</sup> of the physics believed to result in the Jao Gap, in Sec-  
<sup>82</sup> tion 3 we review the differences between OPAL and  
<sup>83</sup> OPLIB and describe how we update DSEP to use  
<sup>84</sup> OPLIB opacity tables. In Section 3.2 we validate the  
<sup>85</sup> update opacities by generating solar calibrated stellar  
<sup>86</sup> models. Section 4 walks through the stellar evolution  
<sup>87</sup> and population synthesis modeling we perform. Finally,  
<sup>88</sup> in Section 5 we present our findings.

## 89           2. JAO GAP

<sup>90</sup> A theoretical explanation for the Jao Gap (Figure 1)  
<sup>91</sup> comes from [van Saders & Pinsonneault \(2012\)](#), who pro-  
<sup>92</sup> pose that in a star directly above the transition mass,  
<sup>93</sup> due to asymmetric production and destruction of  $^3\text{He}$   
<sup>94</sup> during the proton-proton I chain (ppI), periodic lumi-  
<sup>95</sup> nosity variations can be induced. This process is known  
<sup>96</sup> as convective-kissing instability. Very shortly after the  
<sup>97</sup> zero-age main sequence such a star will briefly develop  
<sup>98</sup> a radiative core; however, as the core temperature ex-  
<sup>99</sup> ceeds  $7 \times 10^6$  K, enough energy will be produced by the  
<sup>100</sup> ppI chain that the core once again becomes convective.  
<sup>101</sup> At this point the star exists with both a convective core  
<sup>102</sup> and envelope, in addition to a thin, radiative layer sepa-  
<sup>103</sup> rating the two. Subsequently, asymmetries in ppI affect  
<sup>104</sup> the evolution of the star's convective core.

<sup>105</sup> The proton-proton I chain constitutes three reactions

- <sup>106</sup> 1.  $p + p \rightarrow d + e^+ + \nu_e$
- <sup>107</sup> 2.  $p + d \rightarrow ^3\text{He} + \gamma$
- <sup>108</sup> 3.  $^3\text{He} + ^3\text{He} \rightarrow ^4\text{He} + 2p$

<sup>109</sup> Initially, reaction 3 of ppI consumes  $^3\text{He}$  at a slower  
<sup>110</sup> rate than it is produced by reaction 2 and as a result,  
<sup>111</sup> the core  $^3\text{He}$  abundance and consequently the rate of  
<sup>112</sup> reaction 3, increases with time. The core convective

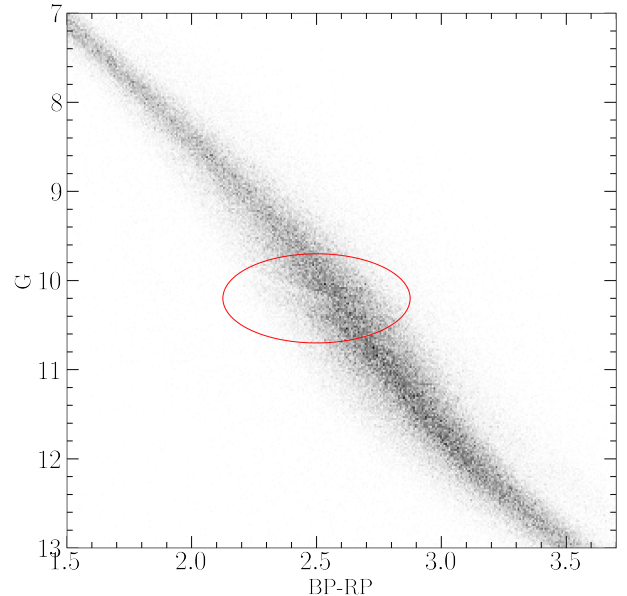


**Figure 1.** The Jao Gap (circled) seen in the Gaia Catalogue of Nearby Stars ([Gaia Collaboration et al. 2021](#)).

<sup>113</sup> zone expands as more of the star becomes unstable to  
<sup>114</sup> convection. This expansion continues until the core con-  
<sup>115</sup> nects with the convective envelope. At this point convec-  
<sup>116</sup> tive mixing can transport material throughout the entire  
<sup>117</sup> star and the high concentration of  $^3\text{He}$  rapidly diffuses  
<sup>118</sup> outward, away from the core, decreasing energy genera-  
<sup>119</sup> tion as reaction 3 slows down. Ultimately, this leads to  
<sup>120</sup> the convective region around the core pulling back away  
<sup>121</sup> from the convective envelope, leaving in place the radia-  
<sup>122</sup> tive transition zone, at which point  $^3\text{He}$  concentrations  
<sup>123</sup> grow in the core until it once again expands to meet  
<sup>124</sup> the envelope. These periodic mixing events will con-  
<sup>125</sup> tinue until  $^3\text{He}$  concentrations throughout the star reach  
<sup>126</sup> an equilibrium ultimately resulting in a fully convective  
<sup>127</sup> star. Figure 2 traces the evolution of a characteristic  
<sup>128</sup> star within the Jao Gap's mass range.

### 129           2.1. Efforts to Model the Gap

<sup>130</sup> Since the identification of the Gap, stellar modeling  
<sup>131</sup> has been conducted to better constrain its location, ef-  
<sup>132</sup> fects, and exact cause. Both [Mansfield & Kroupa \(2021\)](#)  
<sup>133</sup> and [Feiden et al. \(2021\)](#) identify that the Gap's mass lo-  
<sup>134</sup> cation is correlated with model metallicity — the mass-  
<sup>135</sup> luminosity discontinuity in lower metallicity models be-  
<sup>136</sup> ing at a commensurately lower mass. [Feiden et al. \(2021\)](#)  
<sup>137</sup> suggests this dependence is due to the steep relation of  
<sup>138</sup> the radiative temperature gradient,  $\nabla_{rad}$ , on tempera-  
<sup>139</sup> ture and, in turn, on stellar mass.

$$\nabla_{rad} \propto \frac{L\kappa}{T^4} \quad (1)$$

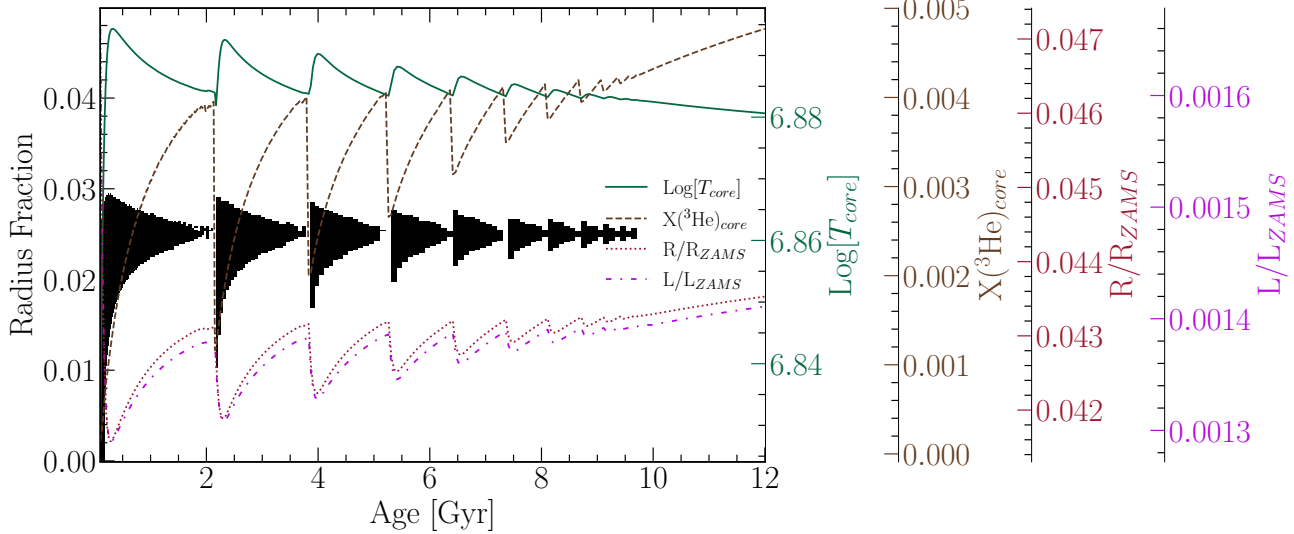


**Figure 2.** Diagram for a characteristic stellar model of  $0.35625 M_{\odot}$  which is within the Jao Gap’s mass range. The black shaded regions denote whether, at a particular model age, a radial shell within the model is radiative (with white meaning convective). The lines trace the models core temperature, core  ${}^3\text{He}$  mass fraction, fractional luminosity wrt. the zero age main sequence and fractional radius wrt. the zero age main sequence.

As metallicity decreases so does opacity, which, by Equation 1, dramatically lowers the temperature at which radiation will dominate energy transport (Chabrier & Baraffe 1997). Since main sequence stars are virialized the core temperature is proportional to the core density and total mass. Therefore, if the core temperature where convective-kissing instability is expected decreases with metallicity, so too will the mass of stars which experience such instabilities.

The strong opacity dependence of the Jao Gap begs the question: **what is the effect of different opacity calculations on Gap properties**. As we can see above, changing opacity should affect the Gap’s location in the mass-luminosity relation and therefore in a color-magnitude diagram. Moreover, current models of the Gap have yet to locate it precisely in the CMD (Feiden et al. 2021) with an approximate 0.16 G-magnitude difference between the observed and modeled Gaps. Opacity provides one, as yet unexplored, parameter which has the potential to resolve these discrepancies.

### 3. UPDATED OPACITIES

Multiple groups have released high-temperature opacities including, the Opacity Project (OP Seaton et al. 1994), Lawrence Livermore National Labs OPAL opacity tables (Iglesias & Rogers 1996), and Los Alamos National Labs OPLIB opacity tables (Colgan et al. 2016). OPAL high-temperature radiative opacity tables in particular are very widely used by current generation isochrone grids (e.g. Dartmouth, MIST, & StarEvol, Dotter et al. 2008; Choi et al. 2016; Amard et al. 2019).

OPLIB opacity tables (Colgan et al. 2016) are not widely used but include the most up-to-date plasma modeling.

While the overall effect on the CMD of using OPLIB compared to OPAL tables is small, the strong theoretical opacity dependence of the Jao Gap raises the potential for these small effects to measurably shift the Gap’s location. We update DSEP to use high temperature opacity tables based on measurements from Los Alamos national Labs T-1 group (OPLIB, Colgan et al. 2016). The OPLIB tables are created with ATOMIC (Magee et al. 2004; Hakel et al. 2006; Fontes et al. 2015), a modern LTE and non-LTE opacity and plasma modeling code. These updated tables were initially created in an attempt to resolve the discrepancy between helioseismic and solar model predictions of chemical abundances in the sun (Bahcall et al. 2005).

OPLIB tables include monochromatic Rosseland mean opacities — composed from bound-bound, bound-free, free-free, and scattering opacities — for elements hydrogen through zinc over temperatures 0.5eV to 100 keV ( $5802 \text{ K} - 1.16 \times 10^9 \text{ K}$ ) and for mass densities from approximately  $10^{-8} \text{ g cm}^{-3}$  up to approximately  $10^4 \text{ g cm}^{-3}$  (though the exact mass density range varies as a function of temperature).

DSEP ramps the Ferguson et al. (2005) low temperature opacities to high temperature opacities tables between  $10^{4.3} \text{ K}$  and  $10^{4.5} \text{ K}$ ; therefore, only differences between high-temperature opacity sources above  $10^{4.5} \text{ K}$  can effect model evolution. When comparing OPAL and OPLIB opacity tables (Figure 3) we find OPLIB opacities are systematically lower than OPAL opacities

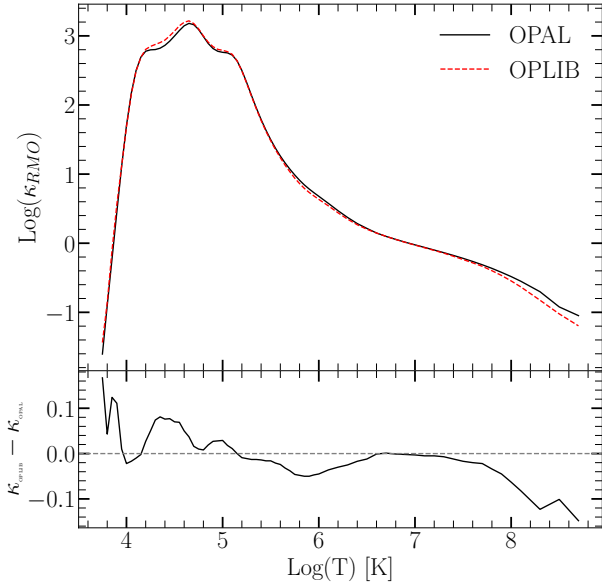


**Figure 3.** Rosseland mean opacity with the GS98 solar composition for both OPAL opacities and OPLIB opacities (top). Residuals between OPLIB opacities and OPAL opacities (bottom). These opacities are plotted at  $\log_{10}(R) = -1.5$ ,  $X = 0.7$ , and  $Z = 0.02$ . Note how the OPLIB opacities are systematically lower than the OPAL opacities for temperatures above  $10^5$  K.

for temperatures above  $10^5$  K. Between  $10^{4.3}$  and  $10^5$  K OPLIB opacities are larger than OPAL opacities. These generally lower opacities will decrease the radiative temperature gradient throughout much of the radius of a model.

### 3.1. Table Querying and Conversion

The high-temperature opacity tables used by DSEP and most other stellar evolution programs give Rosseland-mean opacity,  $\kappa_R$ , along three dimensions: temperature, a density proxy  $R$  (Equation 2;  $T_6 = T \times 10^{-6}$ ,  $\rho$  is the mass density), and composition.

$$R = \frac{\rho}{T_6^3} \quad (2)$$

OPLIB tables may be queried from a web interface<sup>1</sup>; however, OPLIB opacities are parametrized using mass density and temperature instead of  $R$  and temperature. It is most efficient for us to convert these tables to the OPAL format instead of modifying DSEP to use the OPLIB format directly. In order to generate many tables easily and quickly we develop a web scraper which can automatically retrieve all the tables needed to build

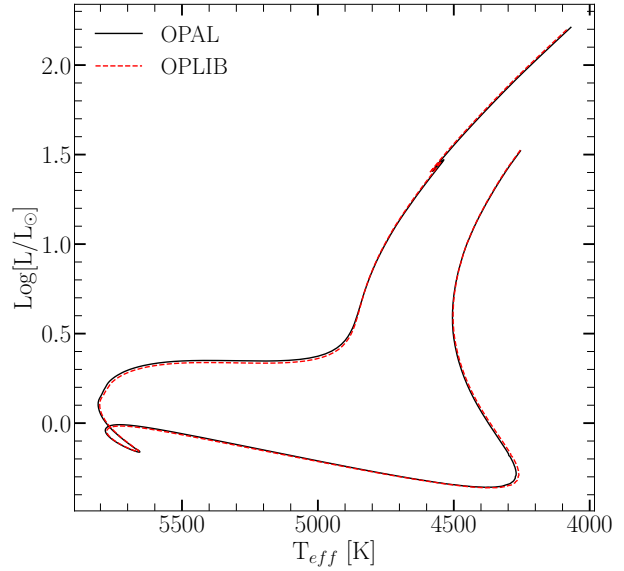


**Figure 4.** HR Diagram for the two SCSMs, OPAL and OPLIB. OPLIB is shown as a red dashed line.

an opacity table in the OPAL format. For a detailed discussion of how OPLIB tables are transformed into a format DSEP can use see Appendix A.

### 3.2. Solar Calibrated Stellar Models

In order to validate the OPLIB opacities, we generate a solar calibrated stellar model (SCSM) using these new tables. We first manually calibrate  $Z/X$  at the model surface to within one part in 100 of the solar value. Subsequently, we allow both the convective mixing length parameter,  $\alpha_{ML}$ , and the initial Hydrogen mass fraction,  $X$ , to vary simultaneously, minimizing the difference, to within one part in  $10^5$ , between resultant models' final radius and luminosity to those of the sun. Finally, we confirm that the model's surface  $Z/X$  abundance is still within one part in 100 of the solar value.

Solar calibrated stellar models evolved using GS98 OPAL and OPLIB opacity tables (Figure 4) differ  $\sim 0.5\%$  in the SCSM hydrogen mass fractions and  $\sim 1.5\%$  in the SCSM convective mixing length parameters (Table 1). While the two evolutionary tracks are very similar, note that the OPLIB SCSM's luminosity is systematically lower past the solar age. While at the solar age the OPLIB SCSM luminosity is effectively the same as the OPAL SCSM. This luminosity difference between OPAL and OPLIB based models is not inconsistent with expectations given the more shallow radiative temperature gradient resulting from the lower OPLIB opacities

## 4. MODELING

In order to model the Jao Gap we evolve two extremely finely sampled mass grids of models. One of

<sup>1</sup> <https://aphysics2.lanl.gov/apps/>

Model	$X$	$\alpha_{ML}$
OPAL	0.7066	1.9333
OPLIB	0.7107	1.9629

**Table 1.** Optimized parameters for SCSMs evolved using OPAL and OPLIB high temperature opacity tables.

these grids uses the OPAL high-temperature opacity tables while the other uses the OPLIB tables (Figure 5). Each grid evolves a model every  $0.00025 M_{\odot}$  from 0.2 to  $0.4 M_{\odot}$  and every  $0.005 M_{\odot}$  from 0.4 to  $0.8 M_{\odot}$ . All models in both grids use a GS98 solar composition, the (1, 101, 0) `FreeEOS` (version 2.7) configuration, and 1000 year old pre-main sequence polytropic models, with polytropic index 1.5, as their initial conditions.

Because in this work we are just interested in the location shift of the Gap as the opacity source varies, we do not model variations in composition. Mansfield & Kroupa (2021); Jao & Feiden (2020); Feiden et al. (2021) all look at the effect composition has on Jao Gap location. They find that as population metallicity increases so too does the mass range and consequently the magnitude of the Gap. From an extremely low metallicity population ( $Z=0.001$ ) to a population with a more solar like metallicity this shift in mass range can be up to  $0.05 M_{\odot}$  (Mansfield & Kroupa 2021).

#### 4.1. Population Synthesis

In order to compare the Gap to observations we use in house population synthesis code. Our population synthesis code first uses inverse CDF sampling to build a distribution of target masses from some initial mass function (IMF). Specifically we use the Sollima (2019) IMF where, for masses  $0.25 M_{\odot} < M < 1 M_{\odot}$ ,  $\alpha = -1.34 \pm 0.07$ . The model nearest in mass to the samples mass above and the nearest model below are then selected from the evolved model database. The surface gravity, luminosity, and effective temperature of the sample are estimated from a linear interpolation between the upper and lower bounding models.  $T_{eff}$ ,  $g$ , and  $\log(L)$  are transformed to Gaia G, BP, and RP magnitudes using the Gaia (E)DR3 bolometric corrections (Creevey et al. 2022) along with code obtained thorough personal communication with Aaron Dotter [How to cite Aaron's color code?]. Next, we introduce observationally informed photometric and astrometric uncertainties into our population.

The full series of steps in our population synthesis code are

$$\sigma_{plx}(M_g) = ae^{bM_g} + c \quad (3)$$

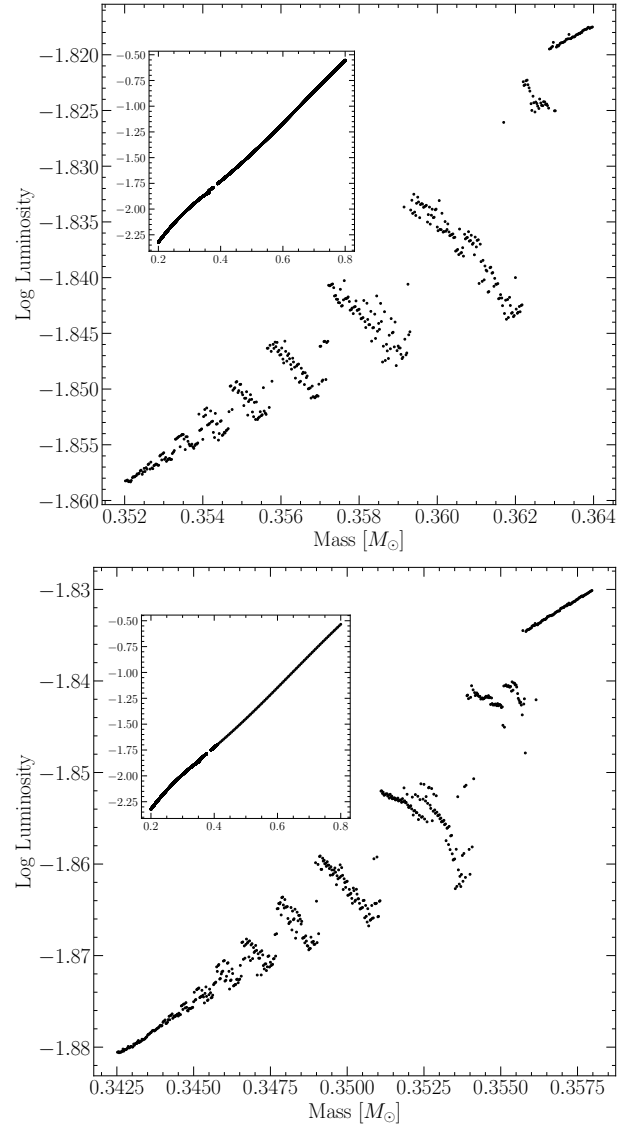


**Figure 5.** Mass-luminosity relation at 7 Gyrs for models evolved using OPAL opacity tables (top) and those evolved using OPLIB opacity tables (bottom). Note the lower mass range of the OPLIB Gap.

$$\sigma_i(M_i) = ae^{M_i - b} + c \quad (4)$$

- Sample from a Sollima (2019) IMF to determine synthetic star mass.
- Find the closest model above and below the synthetic star, linearly interpolate model parameters to the synthetic star mass.
- Convert synthetic star  $g$ ,  $T_{eff}$ , and  $\log(L)$  to Gaia G, BP, and RP magnitudes.

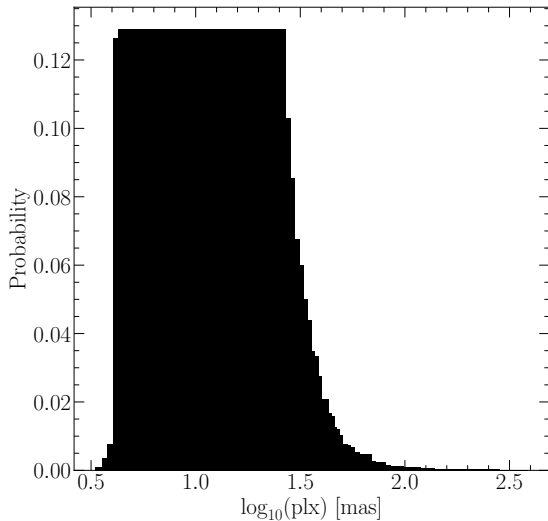


**Figure 6.** Probability distribution sampled when assigning true parallaxes to synthetic stars. This distribution is built from the GCNS and includes all stars with absolute BP-RP colors between 2.3 and 2.9, the same color range of the Jao Gap.

- 307 4. Sample from the GCNS, limited to the absolute  
308 BP-RP color range of 2.3 – 2.9, to assign synthetic  
309 star a “true” parallax.
- 310 5. Use the true parallax to find an apparent magni-  
311 tude for each filter.
- 312 6. Evaluate the empirical calibration given in Equa-  
313 tion 3 to find an associated parallax uncertainty  
314 and adjust the true parallax by this value result-  
315 ing in an “observed” parallax.
- 316 7. Use the “observed” parallax and the apparent  
317 magnitude to find an “observed” magnitude.
- 318 8. Fit the empirical calibration given in Equation 4  
319 to the GCNS and evaluate it to give a magnitude  
320 uncertainty scale in each band.
- 321 9. Adjust each magnitude by an amount sampled  
322 from a normal distribution with a standard devi-  
323 ation of the magnitude uncertainty scale found  
324 in the previous step.

325 This method then incorporates both photometric and  
326 astrometric uncertainties into our population synthe-  
327 sis. An example 7 Gyr old synthetic populations using  
328 OPAL and OPLIB opacities are presented in Figure 7.

Model	Location	Prominence	Width
OPAL 1	10.138	0.593	0.027
OPAL 2	10.183	0.529	0.023
OPLIB 1	10.188	0.724	0.032
OPLIB 2	10.233	0.386	0.027

**Table 2.** Locations identified as potential Gaps.

## 5. RESULTS

329 We quantify the Jao Gap location along the magni-  
330 tude (Table 2) axis by sub-sampling our synthetic pop-  
331 ulations, finding the linear number density along the  
332 magnitude axis of each sub-sample, averaging these lin-  
333 ear number densities, and extracting any peaks above  
334 a prominence threshold of 0.1 as potential magnitudes  
335 of the Jao Gap (Figure 8). Gap widths are measured  
336 at 50% the height of the peak prominence. We use the  
337 python package `scipy` (Virtanen et al. 2020) to both  
338 identify peaks and measure their widths.

340 In both OPAL and OPLIB synthetic populations our  
341 Gap identification method finds two gaps above the  
342 prominence threshold. The identification of more than  
343 one gap is not inconsistent with the mass-luminosity  
344 relation seen in the grids we evolve. As noise is in-  
345 jected into a synthetic population smaller features will  
346 be smeared out while larger ones will tend to persist.  
347 The mass-luminosity relations shown in in Figure 5 make  
348 it clear that there are: (1), multiple gaps due to stars of  
349 different masses undergoing convective mixing events at  
350 different ages, and (2), the gaps decrease in width mov-  
351 ing to lower masses / redder. Therefore, the multiple  
352 gaps we identify are attributable to the two bluest gaps  
353 being wide enough to not smear out with noise. In fact,  
354 if we lower the prominence threshold just slightly from  
355 0.1 to 0.09 we detect a third gap in both the OPAL and  
356 OPLIB datasets where one would be expected.

357 The mean gap location of the OPLIB population is at  
358 a fainter magnitude than the mean gap location of the  
359 OPAL population. Consequently, in the OPLIB sample  
360 the convective mixing events which drive the kissing in-  
361 stability happen more regularly and therefore also start  
362 earlier in the model’s evolution. This is because each  
363 mixing event serves to interrupt the “standard” lumi-  
364 nosity evolution of a stellar model, kicking its luminosity  
365 back down to what it would have been at some earlier  
366 stage of stellar evolution instead of allowing it to slowly  
367 increase.

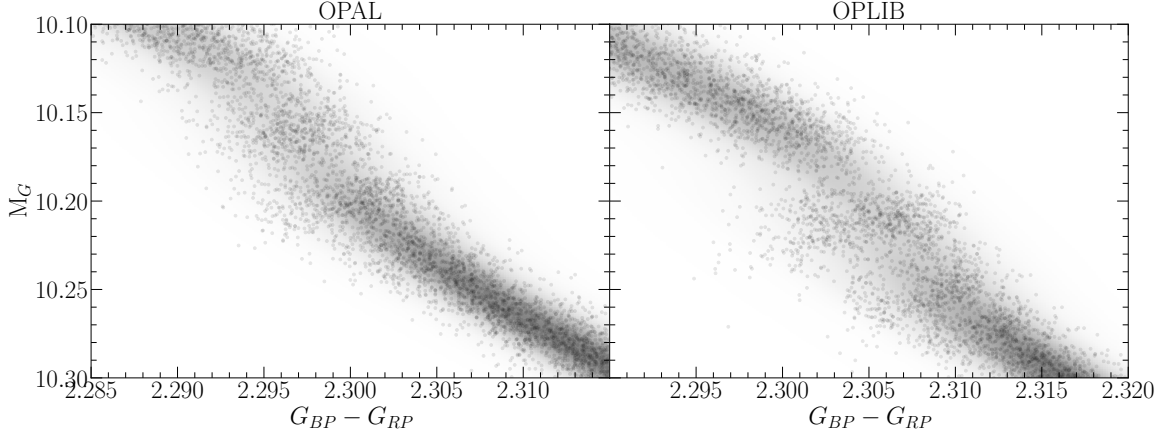


**Figure 7.** Population synthesis results for models evolved with OPAL (left) and models evolved with OPLIB (right). A Gaussian kernel-density estimate has been overlaid to better highlight the density variations.

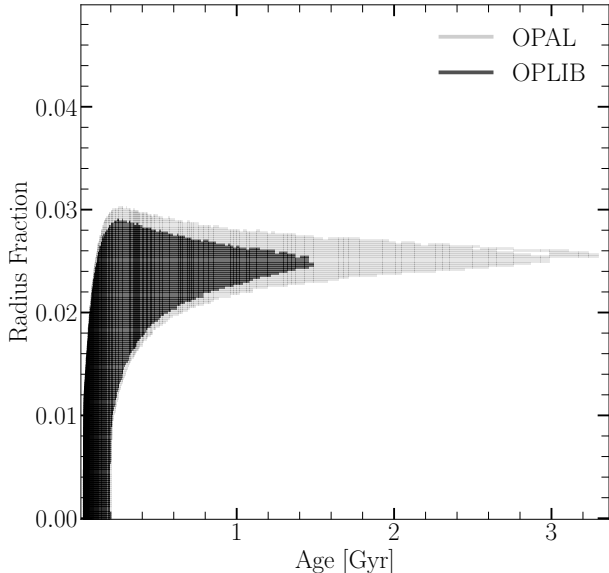


**Figure 9.** Portions of  $0.3526 M_\odot$  OPAL and OPLIB stellar models showing the interior shells which are radiative (black region). Note that for clarity only one convective mixing event from each model is shown. Note how the radiative zone in the OPLIB model is larger.

368 Radially larger radiative zones are consistent with the  
 369 slightly lower opacities characteristic to OPLIB. A lower  
 370 opacity fluid will have a more shallow radiative tempera-  
 371 ture gradient than a higher opacity fluid; however, as the  
 372 adiabatic temperature gradient remains essentially un-  
 373 changed as a function of radius, a larger interior radius  
 374 of the model will remain unstable to radiation (Figure  
 375 9). This thicker radiative zone will extend the time it  
 376 takes the core convective zone to meet up with convec-  
 377 tive envelope. We can additionally see this longer lived  
 378 radiative zone in the core  $^3\text{He}$  mass fraction, in which  
 379 OPLIB models reach much higher concentrations — at

380 approximately the same growth rate — for the same  
 381 mass (Figure 10).  
 382 The most precise published Gap location comes from  
 383 Jao & Feiden (2020) who use EDR3 to locate the Gap  
 384 at  $M_G \sim 10.3$ , we identify the Gap at a similar loca-  
 385 tion in the GCNS data. **The Gap in populations**  
 386 **evolved using OPLIB tables is closer to this mea-**  
 387 **surement than it is in populations evolved using**  
 388 **OPAL tables (Table 2).** It should be noted that the  
 389 exact location of the observed Gap is poorly captured by  
 390 a single value as the Gap visibly compresses across the  
 391 width of the main-sequence, wider on the blue edge and  
 392 narrower on the red edge such that the observed Gap has  
 393 downward facing a wedge shape (Figure 1). This wedge  
 394 shape is not successfully reproduced by either any cur-  
 395 rent models or the modeling we perform here. We elect  
 396 then to specify the Gap location where this wedge is at  
 397 its narrowest, on the red edge of the main sequence.

398 The Gaps identified in our modeling have widths of  
 399 approximately 0.03 magnitudes, while the shift from  
 400 OPAL to OPLIB opacities is 0.05 magnitudes. With  
 401 the prior that the Gaps clearly shift before noise is in-  
 402 jected we know that this shift is real. However, the  
 403 shift magnitude and Gap width are of approximately  
 404 the same size in our synthetic populations. Moreover,  
 405 Feiden et al. (2021) identify that the shift in the mod-  
 406 elled Gap mass from  $[\text{Fe}/\text{H}] = 0$  to  $[\text{Fe}/\text{H}] = +0.5$  as  
 407  $0.04 M_\odot$ , whereas we only see an approximate  $0.01 M_\odot$   
 408 shift between OPAL and OPLIB models. **Therefore,**  
 409 **the Gap location will likely not provide a usable**  
 410 **constraint on the opacity source.**

## 6. CONCLUSION

411 The Jao Gap provides an intriguing probe into the in-  
 412 terior physics of M Dwarfs stars where traditional meth-  
 413 ods of studying interiors break down. However, before

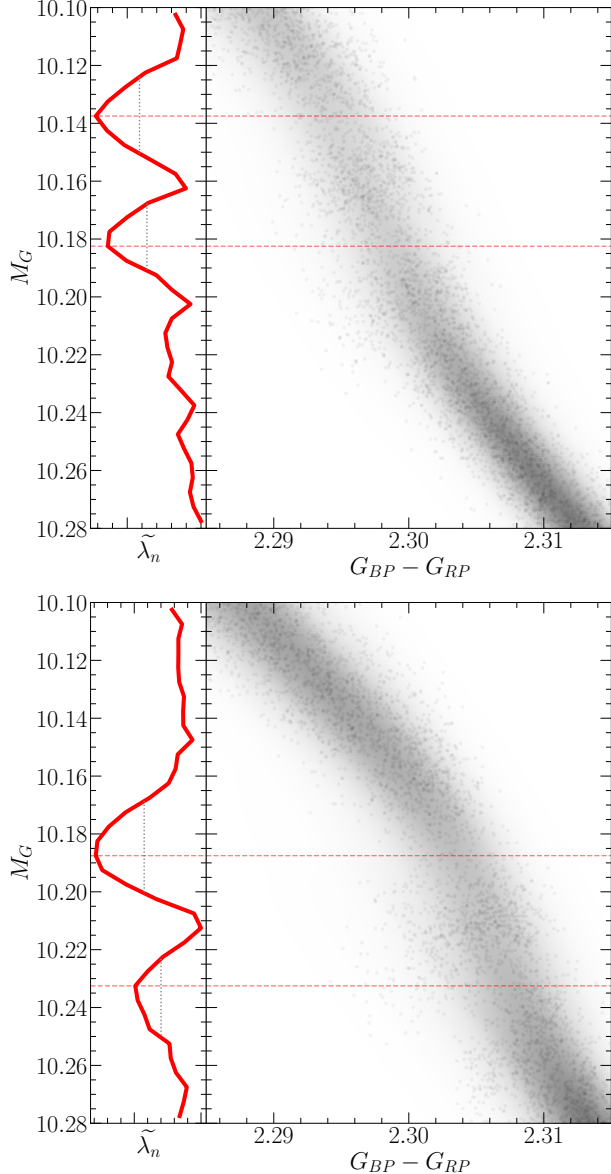


**Figure 8.** (right panels) OPAL (top) and OPLIB (bottom) synthetic populations. (left panels) Normalized linear number density along the magnitude axis. A dashed line has been extended from the peak through both panels to make clear where the identified Jao Gap location is wrt. to the population.

415 detailed physics may be inferred it is essential to have  
 416 models which are well matched to observations. Here  
 417 we investigate whether the OPLIB opacity tables repro-  
 418 duce the Jao Gap location and structure more accurately  
 419 than the widely used OPAL opacity tables. We find that  
 420 while the OPLIB tables do shift the Jao Gap location  
 421 more in line with observations, by approximately 0.05  
 422 magnitudes, the shift is small enough that it is likely  
 423 not distinguishable from noise due to population age

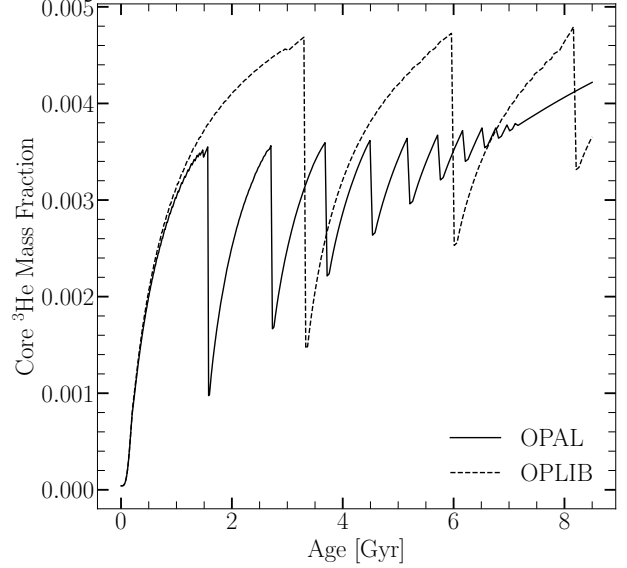


**Figure 10.** Core  ${}^3\text{He}$  mass fraction for  $0.3526 M_{\odot}$  models evolved with OPAL and OPLIB (within the Jao Gap's mass range for both). Note how the OPLIB model's core  ${}^3\text{He}$  mass fraction grows at approximately the same rate as the OPAL model's but continues uninterrupted for longer.

424 and chemical variation. Moreover, we do not find that  
 425 the OPLIB opacity tables help in reproducing the wedge  
 426 shape of the observed Gap.

427

## APPENDIX

428

### A. INTERPOLATING $\rho \rightarrow R$

429 OPLIB reports  $\kappa_R$  as a function of mass density, temperature in keV, and composition. DSEP uses tables where  
 430 opacity is given as a function of temperature in Kelvin,  $R$ , and composition. The conversion from temperature in keV  
 431 to Kelvin is trivial

432

$$T_K = T_{\text{keV}} * 11604525.0061657 \quad (\text{A1})$$

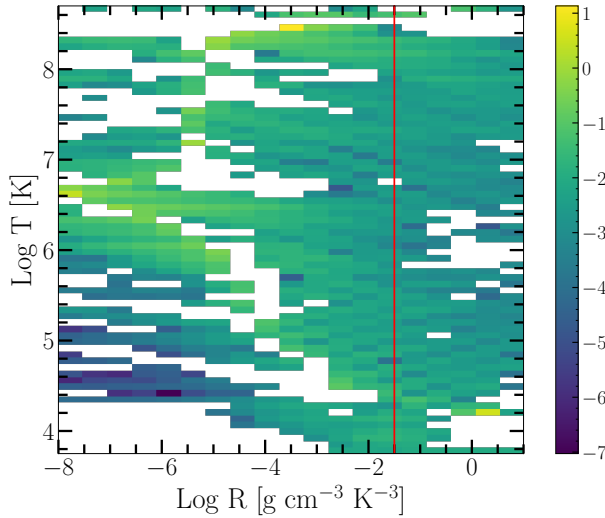


**Figure 11.** Log Fractional Difference between opacities in  $\kappa_R(\rho, T_{eff})$  space directly queried from the OPLIB web-form and those which have been interpolated into  $\log(R)$  space and back. Note that, due to the temperature grid DSEP uses not aligning perfectly with the temperature grid OPLIB uses there may be edge effects where the interpolation is poorly constrained. The red line corresponds to  $\log(R) = -1.5$  where much of a stellar model’s radius exists.

434 However, the conversion from mass density to  $R$  is more involved. Because  $R$  is coupled with both mass density and  
 435 temperature there there is no way to directly convert tabulated values of opacity reported in the OPLIB tables to  
 436 their equivalents in  $R$  space. Instead we must rotate the tables, interpolating  $\kappa_R(\rho, T_{eff}) \rightarrow \kappa_R(R, T_{eff})$ .

437 To preform this rotation we use the `interp2d` function within `scipy`’s `interpolate` (Virtanen et al. 2020) module to  
 438 construct a cubic bivariate B-spline (Dierckx 1981) interpolating function  $s$ , with a smoothing factor of 0, representing  
 439 the surface  $\kappa_R(\rho, T_{eff})$ . For each  $R^i$  and  $T_{eff}^j$  which DSEP expects high-temperature opacities to be reported for,  
 440 we evaluate Equation ?? to find  $\rho^{ij} = \rho(T_{eff}^j, R^i)$ . Opacities in  $T_{eff}$ ,  $R$  space are then inferred as  $\kappa_R^{ij}(R^i, T_{eff}^j) =$   
 441  $s(\rho^{ij}, T_{eff}^j)$ .

442 As first-order validation of this interpolation scheme we can preform a similar interpolation in the opposite direction,  
 443 rotating the tables back to  $\kappa_R(\rho, T_{eff})$  and then comparing the initial, “raw”, opacities to those which have gone  
 444 through the interpolations process. Figure 11 shows the fractional difference between the raw opacities and a set  
 445 which have gone through this double interpolation. The red line denotes  $\log(R) = -1.5$  where models will tend to sit  
 446 for much of their radius. Along the  $\log(R) = -1.5$  line the mean fractional difference is  $\langle \delta \rangle = 0.006$  with an uncertainty  
 447 of  $\sigma_{\langle \delta \rangle} = 0.009$ . One point of note is that, because the initial rotation into  $\log(R)$  space also reduces the domain of the  
 448 opacity function interpolation-edge effects which we avoid initially by extending the domain past what DSEP needs  
 449 cannot be avoided when interpolating back into  $\rho$  space.

450 This work has made use of the NASA astrophysical data system (ADS). We would like to thank Elisabeth Newton,  
 451 Aaron Dotter, and Gregory Feiden for their support and for useful dissussion related to the topic of this paper.  
 452 Additionally, we would like to thank James Colgan for his assistance with the OPLIB opacity tables. We acknowledge  
 453 the support of a NASA grant (No. 80NSSC18K0634).

454 *Software:* The Dartmouth Stellar Evolution Program (Dotter et al. 2008), BeautifulSoup (Richardson 2007),  
 455 mechanize (Chandra & Varanasi 2015)

## REFERENCES

- 456 Amard, L., Palacios, A., Charbonnel, C., et al. 2019, A&A, 588, A77, doi: [10.1051/0004-6361/201935160](https://doi.org/10.1051/0004-6361/201935160)
- 457 Bahcall, J. N., Serenelli, A. M., & Basu, S. 2005, ApJL, 621, L85, doi: [10.1086/428929](https://doi.org/10.1086/428929)

- 460 Baraffe, I., & Chabrier, G. 2018, A&A, 619, A177,  
 461 doi: [10.1051/0004-6361/201834062](https://doi.org/10.1051/0004-6361/201834062)
- 462 Chabrier, G., & Baraffe, I. 1997, A&A, 327, 1039.  
 463 <https://arxiv.org/abs/astro-ph/9704118>
- 464 Chandra, R. V., & Varanasi, B. S. 2015, Python requests  
 465 essentials (Packt Publishing Ltd)
- 466 Choi, J., Dotter, A., Conroy, C., et al. 2016, ApJ, 823, 102,  
 467 doi: [10.3847/0004-637X/823/2/102](https://doi.org/10.3847/0004-637X/823/2/102)
- 468 Colgan, J., Kilcrease, D. P., Magee, N. H., et al. 2016, in  
 469 APS Meeting Abstracts, Vol. 2016, APS Division of  
 470 Atomic, Molecular and Optical Physics Meeting  
 471 Abstracts, D1.008
- 472 Creevey, O. L., Sordo, R., Pailler, F., et al. 2022, arXiv  
 473 e-prints, arXiv:2206.05864.  
 474 <https://arxiv.org/abs/2206.05864>
- 475 Dierckx, P. 1981, IMA Journal of Numerical Analysis, 1,  
 476 267, doi: [10.1093/imanum/1.3.267](https://doi.org/10.1093/imanum/1.3.267)
- 477 Dotter, A., Chaboyer, B., Jevremović, D., et al. 2008, The  
 478 Astrophysical Journal Supplement Series, 178, 89
- 479 Feiden, G. A., Skidmore, K., & Jao, W.-C. 2021, ApJ, 907,  
 480 53, doi: [10.3847/1538-4357/abcc03](https://doi.org/10.3847/1538-4357/abcc03)
- 481 Ferguson, J. W., Alexander, D. R., Allard, F., et al. 2005,  
 482 ApJ, 623, 585, doi: [10.1086/428642](https://doi.org/10.1086/428642)
- 483 Fontes, C. J., Zhang, H. L., Abdallah, J., J., et al. 2015,  
 484 Journal of Physics B Atomic Molecular Physics, 48,  
 485 144014, doi: [10.1088/0953-4075/48/14/144014](https://doi.org/10.1088/0953-4075/48/14/144014)
- 486 Gaia Collaboration, Smart, R. L., Sarro, L. M., et al. 2021,  
 487 A&A, 649, A6, doi: [10.1051/0004-6361/202039498](https://doi.org/10.1051/0004-6361/202039498)
- 488 Hakel, P., Sherrill, M. E., Mazevet, S., et al. 2006, JQSRT,  
 489 99, 265, doi: [10.1016/j.jqsrt.2005.04.007](https://doi.org/10.1016/j.jqsrt.2005.04.007)
- 490 Iglesias, C. A., & Rogers, F. J. 1996, ApJ, 464, 943,  
 491 doi: [10.1086/177381](https://doi.org/10.1086/177381)
- 492 Jao, W.-C., & Feiden, G. A. 2020, AJ, 160, 102,  
 493 doi: [10.3847/1538-3881/aba192](https://doi.org/10.3847/1538-3881/aba192)
- 494 —. 2021, Research Notes of the American Astronomical  
 495 Society, 5, 124, doi: [10.3847/2515-5172/ac053a](https://doi.org/10.3847/2515-5172/ac053a)
- 496 Jao, W.-C., Henry, T. J., Gies, D. R., & Hambly, N. C.  
 497 2018, ApJL, 861, L11, doi: [10.3847/2041-8213/aacdf6](https://doi.org/10.3847/2041-8213/aacdf6)
- 498 Magee, N. H., Abdallah, J., Colgan, J., et al. 2004, in  
 499 American Institute of Physics Conference Series, Vol.  
 500 730, Atomic Processes in Plasmas: 14th APS Topical  
 501 Conference on Atomic Processes in Plasmas, ed. J. S.  
 502 Cohen, D. P. Kilcrease, & S. Mazevet, 168–179
- 503 Mansfield, S., & Kroupa, P. 2021, A&A, 650, A184,  
 504 doi: [10.1051/0004-6361/202140536](https://doi.org/10.1051/0004-6361/202140536)
- 505 Nutzman, P., & Charbonneau, D. 2008, PASP, 120, 317,  
 506 doi: [10.1086/533420](https://doi.org/10.1086/533420)
- 507 Richardson, L. 2007, April
- 508 Rodríguez-López, C. 2019, Frontiers in Astronomy and  
 509 Space Sciences, 6, 76, doi: [10.3389/fspas.2019.00076](https://doi.org/10.3389/fspas.2019.00076)
- 510 Seaton, M. J., Yan, Y., Mihalas, D., & Pradhan, A. K.  
 511 1994, MNRAS, 266, 805, doi: [10.1093/mnras/266.4.805](https://doi.org/10.1093/mnras/266.4.805)
- 512 Skrutskie, M. F., Cutri, R. M., Stiening, R., et al. 2006, AJ,  
 513 131, 1163, doi: [10.1086/498708](https://doi.org/10.1086/498708)
- 514 Sollima, A. 2019, Monthly Notices of the Royal  
 515 Astronomical Society, 489, 2377,  
 516 doi: [10.1093/mnras/stz2093](https://doi.org/10.1093/mnras/stz2093)
- 517 van Saders, J. L., & Pinsonneault, M. H. 2012, ApJ, 751,  
 518 98, doi: [10.1088/0004-637X/751/2/98](https://doi.org/10.1088/0004-637X/751/2/98)
- 519 Virtanen, P., Gommers, R., Oliphant, T. E., et al. 2020,  
 520 Nature Methods, 17, 261, doi: [10.1038/s41592-019-0686-2](https://doi.org/10.1038/s41592-019-0686-2)